Modeling of high-speed, methane-air, turbulent combustion, Part II: Reduced methane oxidation chemistry

Rui Xu [a],[*],[1], Sai Sandeep Dammati [b], Xian Shi [a],[2], Ethan Samuel Genter [a], Zoltan Jozefik [d], Matthew E. Harvazinski [e], Tianfeng Lu [b], Alexei Y. Poludnenko [b],[c], Venkateswaran Sankaran [f], Alan R. Kerstein [g], Hai Wang [a],[*]

[a] Department of Mechanical Engineering, Stanford University, Stanford, CA 94305, USA
[b] School of Mechanical, Aerospace, and Manufacturing Engineering, University of Connecticut, Storrs, CT 06269, USA
[c] Department of Aerospace Engineering, Texas A&M University, College Station, TX 77843, USA
[d] Jacobs Engineering, Edwards AFB, CA 93524, USA
[e] Air Force Research Laboratory, Edwards AFB, CA 93524, USA
[f] Air Force Research Laboratory, Wright Patterson AFB, OH 45433, USA
[g] Consultant, Danville, CA 94526, USA

ARTICLE INFO

ABSTRACT

A reduced, 12-species reaction model (FFCMy-12) is proposed for modeling high-speed turbulent methane flames at high Karlovitz numbers. The model was derived from an early development version (FFCMy) of the 119-species Foundational Fuel Chemistry Model Version 2.0. The reduction was carried out by combining direct species pruning, quasi-steady-state assumption, and reaction lumping, targeting a minimum possible set of species that can capture methane combustion over a wide range of thermodynamic conditions. The performance of the reduced FFCMy-12 is compared to that of a 21-species skeletal reaction model (FFCM1-21) generated through conventional directed relation graph theory (DRG) and DRG-aided sensitivity analysis (DRGASA) algorithms. Model testing starts with legacy combustion properties such as homogeneous ignition delay time, laminar flame speed, and extinction/ignition residence time in a perfectly stirred reactor. More importantly, reduced model testing is extended to three-dimensional direct numerical simulations (DNS) of statistically planar, freely propagating turbulent premixed flames at Karlovitz numbers Ka = 10, 10^2, 10^3, and 10^4, which nominally represent conditions from corrugated flamelets to broken reaction zones. Comparisons are made between the DNS results generated by the two chemical kinetic models with respect to turbulent flame structures, turbulent flame speed, and species distributions. Overall, presented results demonstrate the potential of FFCMy-12 for efficient modeling of the methane flames under highly turbulent mixing conditions characterized by a wide range of Ka. As importantly, the one-dimensional turbulence (ODT) model, developed in the companion paper (Part I), is shown to reproduce adequately the mean values of the local thermochemical states observed in the DNS, and as such, the ODT model is a viable DNS surrogate for testing the accuracy and applicability of a reduced model.

Novelty and significance

We present a 12-species reduced methane oxidation reaction model for the modeling of highly turbulent reacting flows. The reduced model is validated using DNS of premixed turbulent methane-air flames over a wide range of turbulent intensities, from relatively modest corresponding to Karlovitz number Ka = 10 to ultra-high intensities at Ka = 10^4. This represents virtually the entire range of turbulent intensities that could be encountered in any realistic situations. The performance of the 12-species reduced model is evaluated against a 21-species skeletal methane oxidation reaction model. The results show excellent agreement between the two models for DNS at Ka = $10 - 10^3$. The one-dimensional turbulence (ODT) model is also examined over the same conditions and is shown to be an effective DNS surrogate for evaluating chemical kinetic model reductions.

Nomenclature

Acronyms

HRR	Heat release rate
IDT	Ignition delay time
Ka	Karlovitz number
LFS	Laminar flame speed
PSR	Perfectly stirred reactor
Re	Reynolds number

Greek Symbols

η	Kolmogorov length scale
ϕ	Equivalence ratio
τ_{ed}	Large-scale eddy turnover time
τ_{ext}	Extinction residence time in a perfectly stirred reactor
τ_{ign}	Ignition residence time in a perfectly stirred reactor
τ_{idt}	Shock-tube ignition delay time
τ_{res}	Residence time

Roman Symbols

L	Domain length
L_{11}	Integral length scale
M	Mach number
p	Pressure
p_5	Pressure behind a reflected shock wave
S_L	Laminar flame speed
S_T	Turbulent flame speed
T	Temperature
T_5	Temperature behind a reflected shock wave
T_{inl}	Inlet temperature in a perfectly stirred reactor
t	Time
U_L	Turbulent velocity at the scale of the domain length, L
U_{rms}	Root mean square of turbulence velocity fluctuations
x, y, z	Cartesian coordinates
Δx	Computational cell size
$\tilde{Y}$	Normalized mass fraction

Superscripts/subscripts

b	Burned state conditions
u	Unburned state conditions

1. Introduction

High-speed, highly turbulent combustion features strongly coupled dynamics between fluid motions and chemical reactions. Fluid processes, such as flow compression and expansion, turbulent mixing, and flow-wall interactions can significantly modify the underlying local composition and thermodynamic state of the reactive mixture, thus strongly affecting its chemical heat release [1,2]. Such complexity poses challenges in developing accurate yet efficient chemical kinetic models to enable direct numerical simulations (DNS). Available models range from global-reaction-based single- or several-step models to elementary-reaction-based detailed multi-species multi-reaction models. For typical highly turbulent combustion simulations, simple global models generally suffer from unsatisfactory predictability outside their design conditions, while detailed models have yet to allow reasonable computation costs. Therefore, skeletal and reduced chemical kinetic models derived from detailed models emerge as the optimal options for balancing simulation accuracy and efficiency. Skeletal and reduced models have been widely used in turbulent combustion simulations

to study, for example, turbulent flame structures [3–7], the Lewis number effects [8], differential diffusion effects [9,10], fuel and chemistry effects [11–13], flame stretch and thickening [14], transition to distributed burning regime [15,16], and impact of heat release on fluid particle dispersion and turbulent diffusivity [17].

The development of skeletal and reduced models typically involves one or several model reduction methods performed on the parent detailed models. Available methods can be approximately classified into two categories: skeletal reduction and time-scale-based reduction. Skeletal reduction eliminates species and reactions that barely contribute to the prediction of combustion properties of interest. Identification of these species and reactions is achieved through sensitivity analysis [18–20], principal component analysis [21], Jacobian analysis [20], integer programming and optimization [22], flux screening or detailed reduction [23], directed relation graph (DRG) [24–26], DRG with error propagation [27], and DRG-aided sensitivity analysis (DRGASA) [28,29]. Time-scale-based reduction effectively removes fast-evolving species from the model and describes their dynamics through algebraic relations based on other species. Example methods include quasi-steady-state and partial equilibrium approximations [30–40], intrinsic low-dimensional manifolds (ILDM) [41], and computational singular perturbation (CSP) [42–45]. A model is typically referred to as skeletal if it was developed only using skeletal reduction methods, while a reduced model results from both skeletal and time-scale-based methods.

In this paper, we introduce a 12-species reduced reaction model named FFCMy-12, which initially targets the reaction chemistry for applications in methane-oxygen rocket combustors. FFCMy-12 is derived based on a 119-species development version of the Foundational Fuel Chemistry Model Version 2.0 [46–48] and a 21-species skeletal model of the Foundational Fuel Chemistry Model Version 1.0 [49,50]. We will refer to the two base models as FFCMy-full and FFCM1-21, respectively.

The development of FFCMy-12 utilizes several aforementioned model reduction methods. Its performance is tested over a wide range of thermodynamic and transport conditions for both methane-oxygen and methane-air combustion, and it is compared to the results of other skeletal and detailed models. A comprehensive set of model validations is carried out. First, predictions from FFCMy-12 are compared to base model predictions for legacy combustion properties, including ignition delay times, laminar flame speeds, and extinction and ignition times in perfectly stirred reactors (PSR). Second, the capability of the model to capture chemical equilibrium is demonstrated through simulations of high-speed expansion flows inside diverging rocket nozzles, comparing the reduced and base models. Third, turbulent combustion properties, including turbulent flame speed, heat release rate, and distributions of species mass fractions are evaluated through DNS of freely propagating premixed flames at various turbulent intensity levels. In particular, DNS compare the model performance between FFCMy-12 and FFCM1-21. Lastly, one-dimensional turbulence (ODT) modeling using FFCMy-12 is presented to demonstrate and highlight the ODT model as a tool for assessing the applicability of a reduced reaction model for simulations of turbulent flames (cf. the companion Part I article [51]). In general, such flames produce large thermochemical state spaces, which can extend beyond the legacy combustion properties that are available for reduced model development.

2. Computational methodology

Computations of ignition delay time (IDT), laminar flame speed (LFS), and extinction and ignition times in perfectly stirred reactor (PSR) were performed using the CHEMKIN package [52]. IDT was calculated using SENKIN [53] assuming constant-volume and adiabatic reactors. The onset of ignition was defined as the time corresponding to the maximum time derivative of pressure. LFS was calculated using PREMIX [54] with the multicomponent transport and thermal diffusion. Extinction and ignition residence times in PSR were obtained
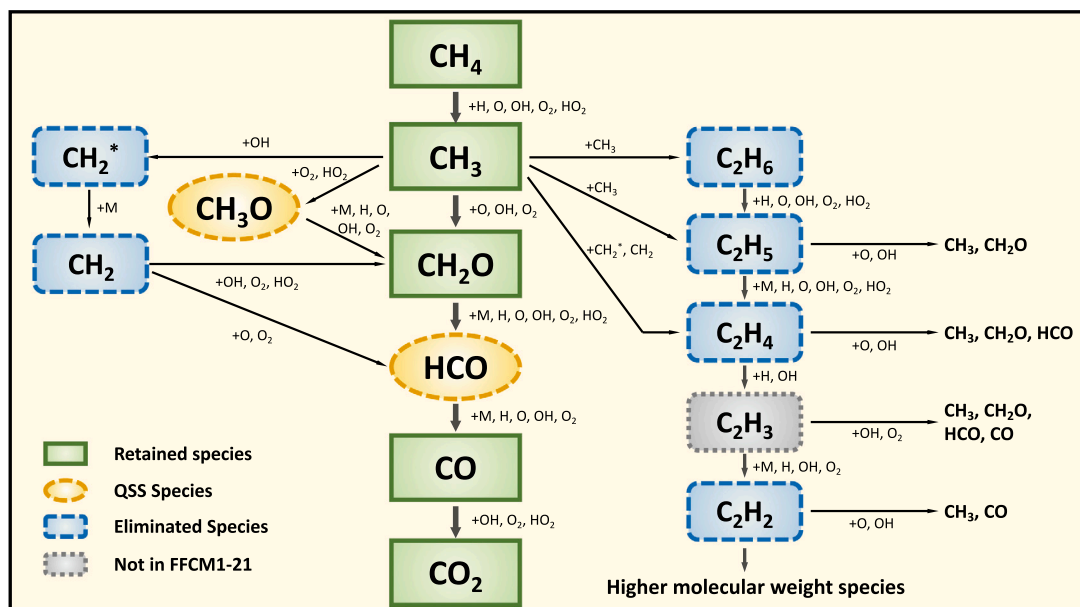
Fig. 1. Reaction pathway diagram of the high-temperature methane oxidation (modified from Law [56] and Warnatz [57]). Only C_1 and C_2 species from FFCM1-21 are shown (excluding H_2 oxidation reaction set and H_2CC).

Table 1
Thermodynamic conditions considered for FFCMy-12 model reduction and validation.

	p (atm)	T^a (K)	ϕ (CH_4–O_2)
IDT	10–100	1200–1800	0.5–2.0
LFS	10–100	298	0.5–2.0
PSR	10–100	298	0.25 & 0.5

[a] Temperature stands for: the initial temperature behind the reflected shock wave for IDT (i.e., T_5), the unburned gas temperature for LFS (i.e., T_u), and the inlet unburned gas temperature for PSR (i.e., T_{inl}).

Table 2
List of the DNS parameters.

Ka	10^1	10^2	10^3	10^4
L_x [mm]	0.671	0.671	0.671	0.168
L_y [mm]	0.671	0.671	0.671	0.168
L_z [mm]	10.74	10.74	5.37	1.34
Δx [μm]	2.6	2.6	1.3	0.33
τ_{ed} [μs]	310.66	67.401	14.527	1.245
$\eta_u/\Delta x$	2.5	0.77	0.5	0.6
$\eta_b/\Delta x$	9.92	3.15	2.0	2.42
L_{11} [mm]	0.158	0.158	0.158	0.040
$Re_u(L_{11})$	110	512	2,545	1,779
$Re_b(L_{11})$	17	81	401	280
U_{rms} [m/s]	2.46	11.41	53.21	155.57

by calculating the *S*-curve [55]. The extinction time was defined as the reaction time corresponding to the upper turning point of the *S*-curve, while the ignition residence time was defined at the lower turning point. Methane-oxygen (CH_4-O_2) mixtures were tested, with the specific compositions and conditions given in Table 1.

Computations of rocket nozzle expansion flows were performed using an in-house developed numerical model. The model solves the one-dimensional, steady-state, and multi-component Euler equations with varying cross-sectional areas and chemical kinetics. Thermodynamic properties and kinetic rate parameters are evaluated using Cantera [58]. Mixtures of CH_4-O_2 were tested at relevant rocket combustion conditions. Details of the numerical model, including governing equations, numerical setup, and a series of model tests are included in the Supplementary Materials (SM) Section S3.

DNS of the three-dimensional (3D), statistically-planar, freely-propagating turbulent premixed flames were performed using the Athena-RFX code [59]. The numerical flow solver in Athena-RFX [59] uses a directionally unsplit corner transport upwind (CTU) finite volume scheme with piecewise parabolic interpolation to achieve 3rd-order spatial and 2nd-order temporal accuracy. Additional details can be found in the companion paper [51] and in Ref. [59]. In DNS, the initial unburned mixture is CH_4-air with the equivalence ratio of 0.7 at 700 K and 30 atm. Cases with four Karlovitz numbers Ka = 10, 10^2, 10^3, and 10^4 are considered. The computational domain size is L_x (transverse) $\times$ L_y (transverse) $\times$ L_z (streamwise), discretized with a uniform mesh size of Δx. To initialize the calculation, computational domain with periodic boundary conditions is filled with the unburned mixture. To create and sustain the turbulence in the domain, a spectral method [59,60] is used to add isotropic, solenoidal (divergence-free) large-scale perturbations to the velocity field. The simulation is then carried out for two large-scale eddy turnover times, $2\tau_{ed}$, to reach a statistically steady state. Here we define $\tau_{ed} = L/U_L$ as the ratio of the domain width, L, to the corresponding turbulent velocity at the scale of the domain width, U_L. Next, the laminar flame structure, namely temperature, density and velocity (assuming isobaric conditions), as well as composition for the same CH_4-air mixture obtained with CHEMKIN PREMIX [54] are superimposed onto the established turbulent velocity field in the DNS domain along the streamwise direction. At the same time, the streamwise boundary conditions are changed from periodic to zero-order extrapolation to avoid pressure build-up. The simulation then continues for another large-scale eddy turnover time to allow the flame to become fully developed before statistics are collected for combustion property analysis.

Table 2 summarizes the parameters used in the DNS calculations at different Ka numbers, including the computational domain size, L_x, L_y, and L_z; cell size, Δx; the large-scale eddy turnover time, τ_{ed}; Kolmogorov length scale in the unburned, η_u and burned mixtures, η_b; the integral length scale, L_{11}; integral-scale Reynolds number, $Re_u(L_{11})$ and $Re_b(L_{11})$; and the root mean square of turbulent velocity fluctuations, U_{rms}. In addition to DNS, a set of simulations using one-dimensional turbulence (ODT) model are also performed to evaluate the performance of the reduced model for large-eddy simulations (LES). The setup for ODT simulations is also described in the companion paper [51], and we do not elaborate it here.
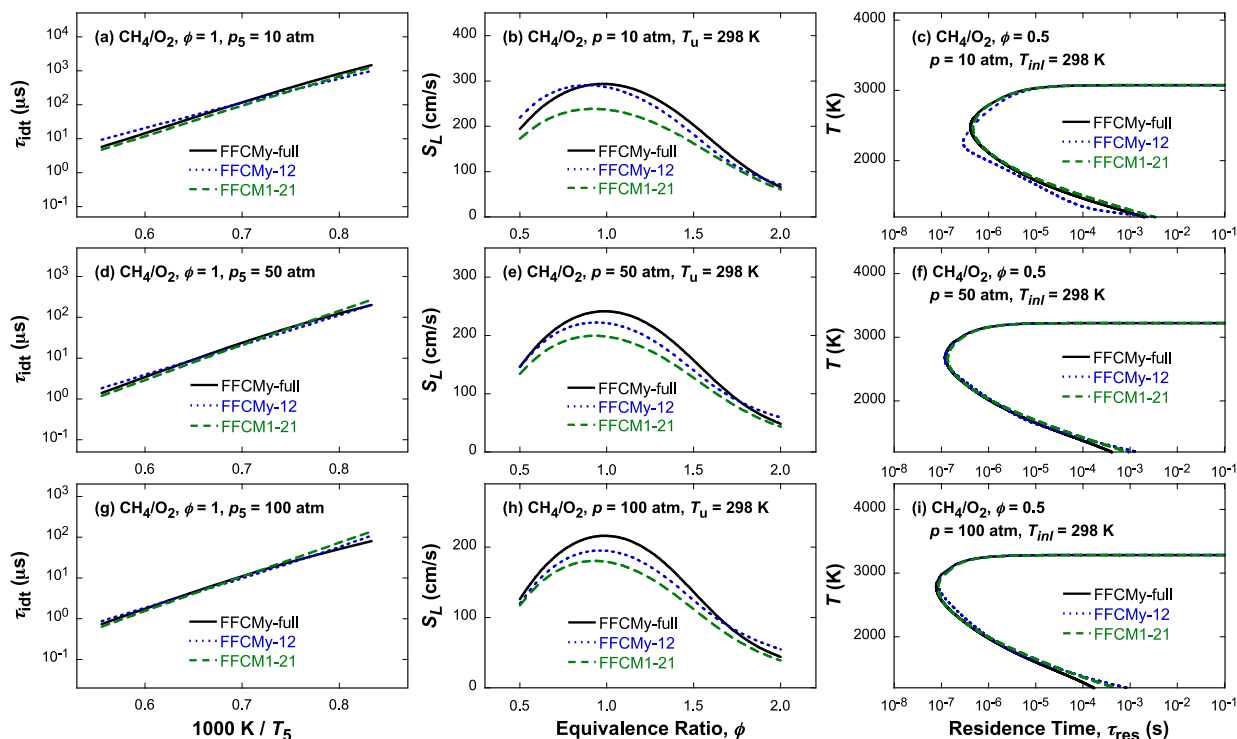
Fig. 2. Comparisons of the calculated ignition delay time, τ_{idt} (left panels a, d, g), laminar flame speed, S_L (middle panels b, e, h), and the temperature S-curve in a perfectly stirred reactor (right panels c, f, i) for the CH_4-O_2 mixture at conditions specified in each panel. Solid lines: FFCMy-full model; dotted lines: FFCMy-12 reduced model; dashed lines: FFCM1-21 skeletal model.

3. FFCMy-12: The reduced methane combustion model

In this section, we describe the model reduction methodology of FFCMy-12, and we demonstrate its performance compared to FFCM1-21, the 21-species skeletal model derived from FFCM1 using the classical DRG/DRGASA method [24,29,40]. Both FFCMy-12 and FFCM1-21 were originally developed for CH_4-O_2 combustion in rocket propulsion applications. Details of FFCM1-21 can be found in Supplementary Materials (SM) Section S1. Good accuracy was achieved, with a maximum relative error of 18% compared to the full FFCM1 model for all test cases, which included ignition delay times, laminar flame speeds, and PSR extinction residence times.

FFCMy-12 is derived based on the FFCMy-full [61], an early development version of the Foundational Fuel Chemistry Model Version 2.0 [46–48]. Fig. 1 shows the reaction pathway diagram of the high-temperature methane oxidation (modified from Law [56] and Warnatz [57]) including only the C_1 and C_2 species. We first reduce the detailed FFCMy-full model to a skeletal set, which contains the same 21 species as in FFCM1-21. Table 3 lists these 21 species (same as in FFCM1-21) with the underlined species being the ones further removed from FFCMy-12. In particular, starting from this 21-species set, we first eliminate all the C_2 species and their respective reactions. Next, singlet and triplet methylene species, i.e., CH_2^* and CH_2, respectively, are eliminated due to their relatively low concentrations. Quasi-steady-state (QSS) assumption is then applied to two species, i.e., HCO and CH_3O (both highlighted in Fig. 1), as their dissociation processes can be facile during the high-temperature combustion process. In doing so, when occurring as reaction products, HCO and CH_3O are directly replaced by their prompt dissociation fragments, namely $HCO \Rightarrow CO + H$ and $CH_3O \Rightarrow CH_2O + H$. For example, an original reaction $CH_2O + O \rightleftharpoons OH + HCO$ can be reformulated as $CH_2O + O \Rightarrow OH + H + CO$, which lumps the fast irreversible HCO dissociation into the product. Under this assumption, the corresponding reverse association reaction $CO + H \Rightarrow HCO$ is not as competitive as the dissociative channel, thereby allowing the corresponding total reactions to be considered as forward

Table 3
Species contained in the FFCM1-21 skeletal model with the underlined species excluded from FFCMy-12.

Chemistry set	Species
H_2	H_2, H, O_2, O, OH, H_2O, HO_2, $\underline{H_2O_2}$
C_1	CH_4, CH_3, $\underline{CH_2}$, CO, CO_2, $\underline{HCO}$, $\underline{CH_2O}$, $\underline{CH_3O}$
C_2	$\underline{C_2H_6}$, $\underline{C_2H_5}$, $\underline{C_2H_4}$, $\underline{C_2H_2}$, $\underline{H_2CC}$

irreversible. Reactions that were treated with the HCO and CH_3O QSS assumption are listed in SM Section S2, Table S1. Lastly, H_2O_2 and its reactions are pruned from the H_2-O_2 oxidation reaction set.

The reduction methodology discussed above, including direct species pruning from the skeletal model and QSS treatment, will inevitably result in a loss of the model accuracy. To tailor the reduced model towards CH_4-O_2 combustion in rocket propulsion applications, reaction rate coefficients of FFCMy-12 are optimized using the results of FFCMy-full as optimization targets, including standard combustion properties such as the ignition delay time, laminar flame speed, and perfectly stirred reactor S-curves. Targeted mixture compositions and thermodynamic conditions are listed in Table 1. Comparison between the optimized and the original rate coefficients are summarized in SM Section S2, Table S1. Fig. 2 shows selected comparisons between the combustion properties of CH_4-O_2 obtained with the FFCMy-12 and FFCMy-full mechanisms, which demonstrates that the final, optimized, reduced FFCMy-12 model is capable of retaining the accuracy of its respective detailed model.

We also examined the performance of FFCMy-12 for the CH_4-air mixtures using the same standard combustion properties. Fig. 3 compares the results obtained with FFCMy-12 and FFCM1-21 for the CH_4-air mixture under the same high-pressure, high-temperature lean conditions considered in the DNS. Some discrepancies are observed. In particular, for the highest initial unburned mixture temperature (Fig. 3a), FFCMy-12 predicts the IDT nearly twice as large as that predicted by FFCM1-21. An opposite trend is observed at lower reactant
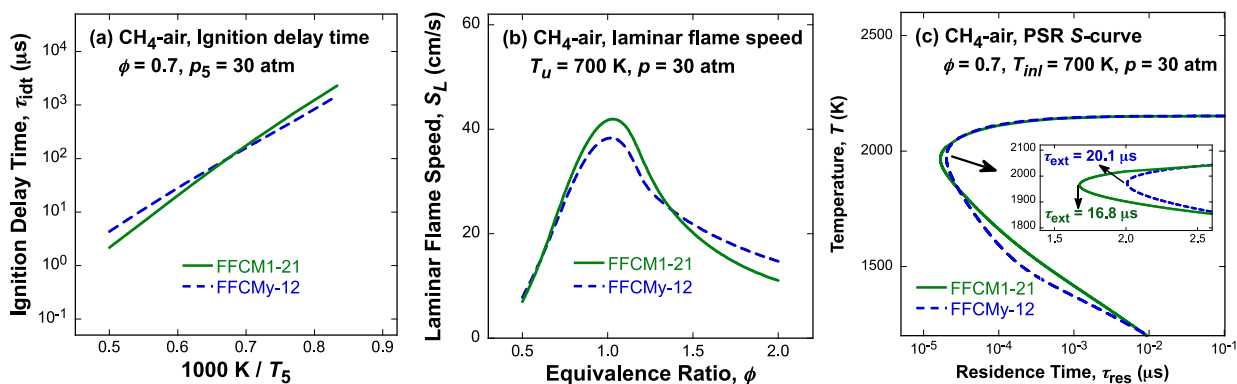
Fig. 3. Comparisons of the calculated (a) ignition delay time, τ_{idt}, (b) laminar flame speed, S_L, and (c) the temperature S-curve in a perfectly stirred reactor for the CH_4-air mixture at conditions considered in the DNS discussed here. Solid lines: FFCM1-21 skeletal model; dashed lines: FFCMy-12 reduced model. The inset in panel c shows the extinction time (τ_{ext}) near the S-curve turning point.
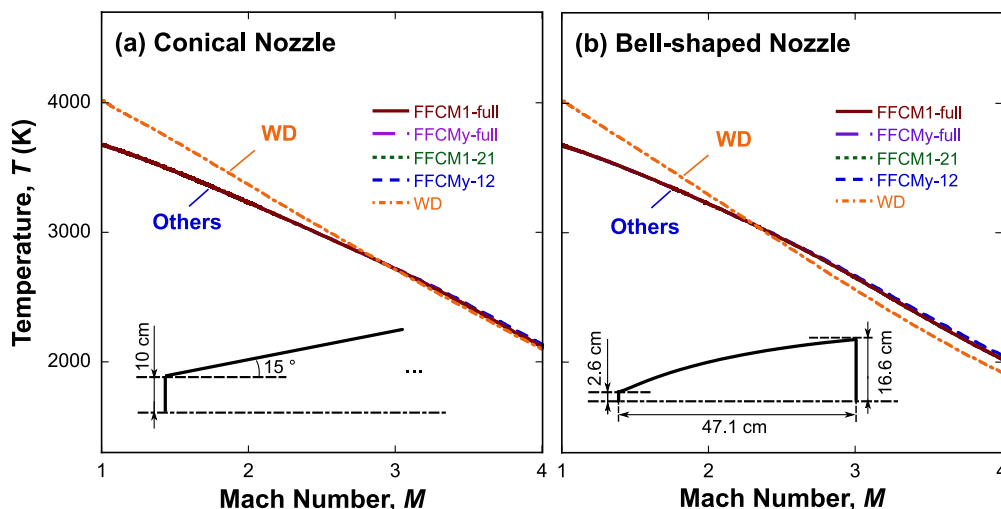

Fig. 4. Comparisons of the temperature as a function of Mach number for the CH_4-O_2 burned mixture expansion in (a) a conical and (b) a bell-shaped rocket nozzle at the following unburned conditions: equivalence ratio $\phi = 1.0$, temperature 700 K, and pressure 60 atm. Results are shown for several chemical kinetic models described in the text. The nozzle geometries are shown in the insets and also in Fig. S5.

temperatures. For the laminar flame speeds, FFCMy-12 results match those of FFCM1-21 for lean mixtures, but they deviate for stoichiometric and rich mixtures. Lastly, the extinction residence times predicted by FFCMy-12 are $\approx 20\%$ higher than those predicted by FFCM1-21. Some of these discrepancies will be discussed later in the DNS result section.

FFCMy-12 is also tested using expansion flow simulations in the typical rocket nozzle configurations. Accurate predictions of chemical equilibrium and near-equilibrium chemical kinetics are crucial for determining the temperature variation during flow expansion due to significant recombination processes. FFCMy-12 was tested against four other chemical kinetic models: FFCM1-full model [49], FFCMy-full model [61], FFCM1-21 skeletal model, and a 3-step global chemistry model by Westbrook and Dryer [62]. The CH_4-O_2 mixtures at lean, stoichiometric, and rich compositions and unburned conditions of 60 atm and 700 K are tested in both a conical nozzle and a bell-shaped nozzle. The calculated temperatures for the stoichiometric mixture are shown in Fig. 4, with the axial Mach number as x-axis. For the equilibrium temperature at the nozzle throat ($M = 1$), the Westbrook-Dryer (WD) model prediction is 10% higher than the rest of the models, which all give similar values. As the temperature drops due to expansion, effect of finite-rate chemical kinetics starts to interplay with the flow time scale, thereby causing the predicted temperature to deviate slightly from

the temperature computed purely based on chemical equilibrium (see SM Fig. S7). Nevertheless, compared to other models, the WD model showed a faster decrease in temperature, as it does not consider radical species such as H, OH, O, and HO_2. Those radicals undergo exothermic recombination reactions during isentropic expansion, forming stable combustion products and releasing heat. In contrast, FFCMy-12 (as well as the skeletal FFCM1-21) takes into account relevant radical recombination kinetics, thus predicting almost identical temperature profiles as those of the two detailed models. Overall, the results shown in Fig. 4 demonstrate the capability of FFCMy-12 to capture the high-speed nozzle flow dynamics with chemical re-equilibration. Further details of the rocket nozzle calculations can be found in SM Section S3, including the description of the numerical formulation, comparisons between the chemical equilibrium and finite-rate kinetics, as well as the additional results for lean and rich mixtures, and comparisons to two additional models GRI-Mech 3.0 [63] and USC Mech II [64].

Finally, FFCMy-12 is tested for the induction and exothermic lengths in methane-oxygen detonations (see SM Section S4). Overall, the reduced model reproduces these characteristic detonation scales in close agreement with the predictions of the detailed FFCM1 and skeletal FFCM1-21 models for the equivalence ratios in the range of 0.7–1.3. Both the FFCMy-12 and FFCM1-21 model files in the Cantera format are available in the Supplementary Materials.
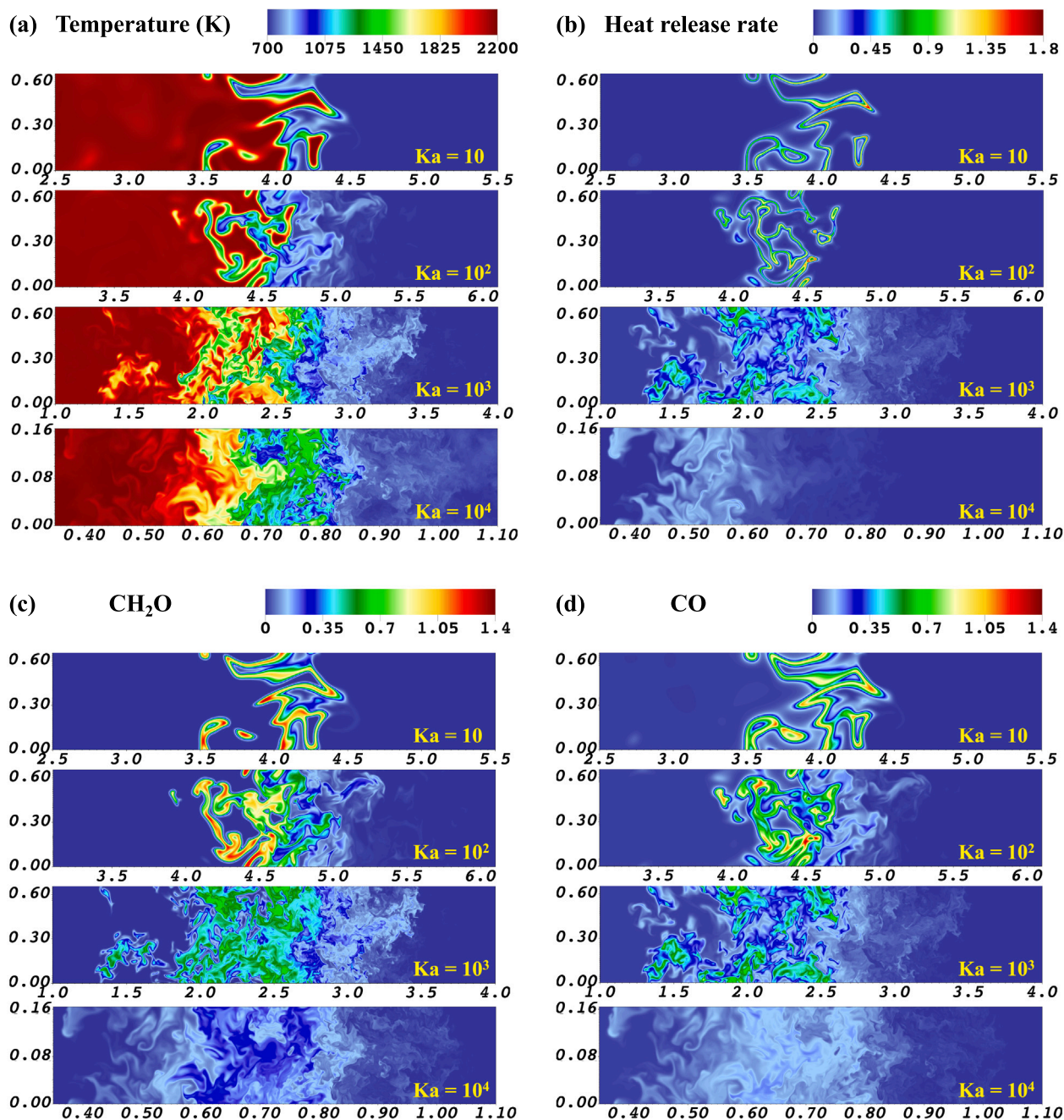
Fig. 5. Distributions of (a) temperature, (b) heat release rate (HRR), (c) CH_2O mass fraction ($\tilde{Y}_{CH_2O}$), and (d) CO mass fraction ($\tilde{Y}_{CO}$) in DNS of the CH_4-air flames calculated using FFCMy-12 at 30 atm, 700 K, and $\phi = 0.7$ for Ka = 10, 10^2, 10^3, and 10^4, respectively. All quantities, except for temperature, are normalized by the peak values in the laminar premixed flame profile calculated for the instantaneous upstream flow pressure and temperature, namely the normalization values are (b) 7.6×10^{14} erg/g·s (Ka = 10), 7.9×10^{14} erg/g·s (Ka = 10^2), 8.0×10^{14} erg/g·s (Ka = 10^3), and 8.8×10^{14} erg/g·s (Ka = 10^4), (c) 2.2×10^{-3}, and (d) 1.7×10^{-2}. All distributions are shown as two-dimensional slices through the middle of the computational domain. Note that the computational domain for the Ka = 10^4 case is four times smaller than at lower Ka.

4. Results and discussion

4.1. Comparison of FFCMy-12 and FFCM1-21 using DNS

Accuracy of the 12-species reduced FFCMy-12 model was first assessed by comparing it to the skeletal FFCM1-21 in DNS of freely propagating, premixed CH_4-air flames at Ka = 10, 10^2, 10^3, and 10^4. The tested Ka numbers represent a wide range of turbulent combustion regimes from low-speed, corrugated flamelets (Ka = 10) to broken reaction zones (Ka = $10^3 - 10^4$). We compare the flame structures,

heat release rates, turbulent flame speeds, and species mass fraction distributions between the two models.

Fig. 5 shows the DNS results for the FFCMy-12 model for all four Ka number cases, namely the two-dimensional (2D) distributions of temperature, normalized heat release rate (HRR) per unit volume, and normalized mass fractions of CH_2O, $\tilde{Y}_{CH_2O}$, and CO, $\tilde{Y}_{CO}$, in the midplane of the computational domain. The effect of varying Ka number on the turbulent flame structure can be seen in the temperature fields (Fig. 5a). At low Ka = 10, the turbulent flame is structured as corrugated flamelets. As Ka increases, the turbulent flame expands and it becomes increasingly more disrupted by turbulent mixing. No clear
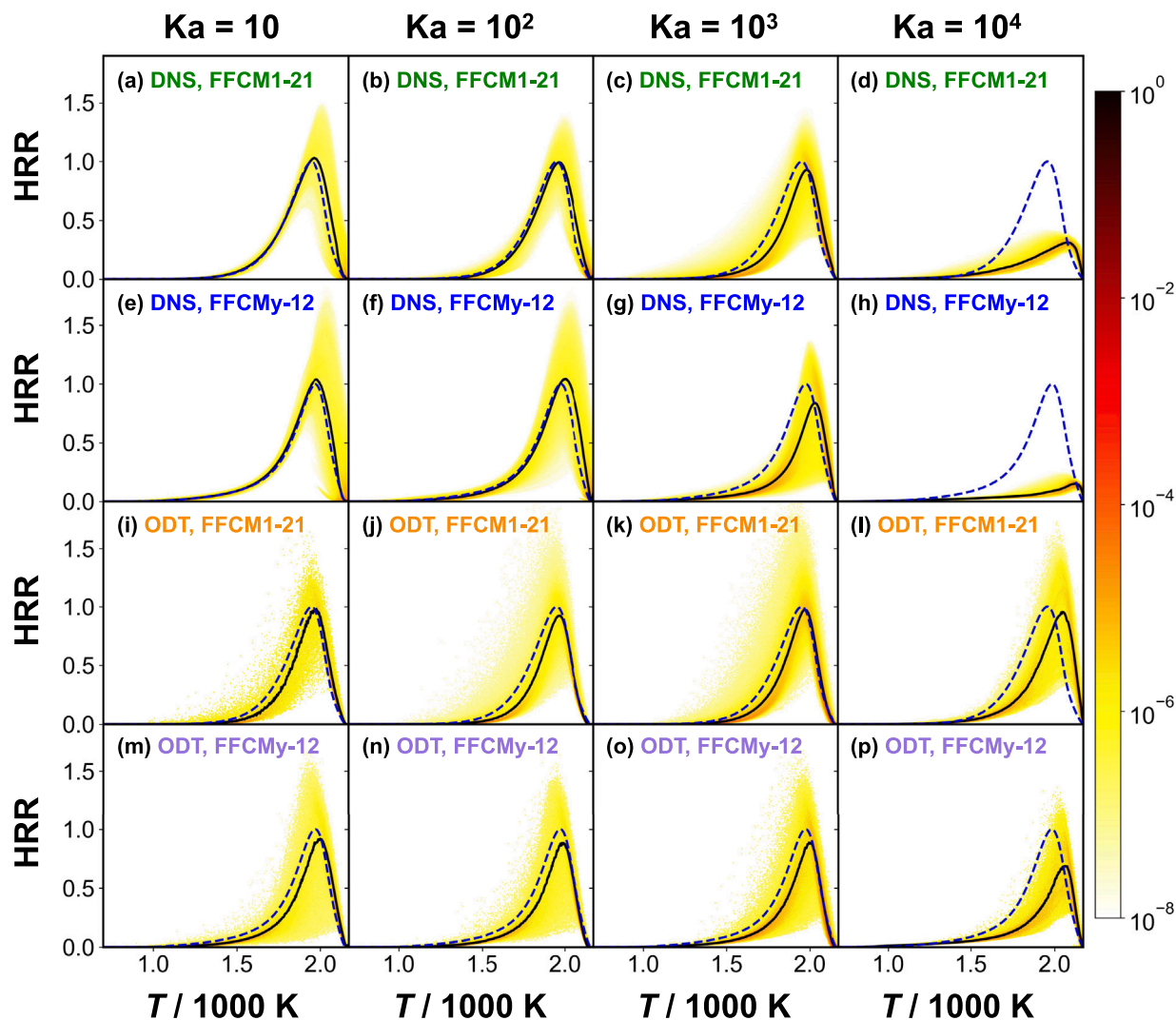
Fig. 6. Joint probability density function (jPDF) of the normalized heat release rate (HRR) vs. temperature obtained from DNS with FFCM1-21 (first row, panels a–d), DNS with FFCMy-12 (second row, panels e–h), ODT with FFCM1-21 (third row, panels i–l), and ODT with FFCMy-12 (bottom row, panels m–p). The jPDF is computed at Ka = 10 (first column, panels a, e, i, m), Ka = 10^2 (second column, panels b, f, j, n), Ka = 10^3 (third column, panels c, g, k, o), and Ka = 10^4 (fourth column, panels d, h, l, p), respectively. Solid lines: mean of the jPDF; dashed lines: results obtained from the laminar premixed flame computation.

flame front can be identified in the highest intensity cases Ka = 10^3 and 10^4. Similar trends are observed for HRR (Fig. 5b), $\tilde{Y}_{CH_2O}$ (Fig. 5c), and $\tilde{Y}_{CO}$ (Fig. 5d) for Ka from 10 to 10^3.

Case Ka = 10^4 shows several differences relative to the lower intensity cases. While the flame width becomes even broader, as indicated by the temperature field (Fig. 5a), chemical reactivity is diminished as the peak values of HRR (Fig. 5b), $\tilde{Y}_{CH_2O}$ (Fig. 5c), and $\tilde{Y}_{CO}$ (Fig. 5d) are much lower compared to those in the Ka = 10^3 case. Possible reasons for this are addressed in the companion paper [51]. Importantly, the 12-species FFCMy-12 mechanism reproduces quite closely the local flame structure predicted using FFCM1-21, as can be seen by comparing the current Fig. 5 with Fig. 2 of the companion paper [51].

Fig. 6 shows the joint probability density function (jPDF) and the mean values for the distributions of heat release rates as a function of temperature. Four sets of simulations are shown, and the results are organized into four rows: from top to bottom are DNS with FFCM1-21, DNS with FFCMy-12, ODT with FFCM1-21, and ODT with FFCMy-12. 1D laminar flame results are also included as a reference. For all four sets of simulations, jPDF exhibit a considerable degree of scatter. For DNS, both models suggest that at Ka = 10 and 10^2, the mean HRR largely agrees with the laminar flame result, while it becomes slightly

smaller than the laminar flame HRR at Ka = 10^3 and substantially smaller at 10^4. This suggests that the most intensive burning occurs between Ka = 10^2 and 10^3 for this particular CH_4-air turbulent flame. For higher Ka, turbulent mixing suppresses heat release, as the turbulent mixing time scale becomes shorter than the chemical reaction time scale leading to weakened chemical reactivity and frequent local extinctions. This is illustrated in Figs. 6d and 6h, which show that the mean peak HRR at Ka = 10^4 decrease to $\approx$ 10–20% of the corresponding laminar premixed flame value. The scatter in the jPDF also shows that HRR can reach values, which are orders of magnitude lower than in the laminar premixed flame, indicating local flame extinctions. ODT results will be discussed later.

The effect of the Ka number on the flame can also be seen in the evolution of the turbulent flame speed, S_T. Fig. 7 shows the DNS and ODT results for both models. We will focus on the DNS results here and discuss the ODT results later. In DNS, S_T is calculated based on the fuel consumption rate [59] and it is normalized by the time-dependent laminar flame speed, $S_L(t)$. The $S_L(t)$ is computed based on the instantaneous mean pressure and temperature of the reactants to account for fuel heating induced by the turbulent energy dissipation, which can be significant at high Ka number conditions. Overall, DNS
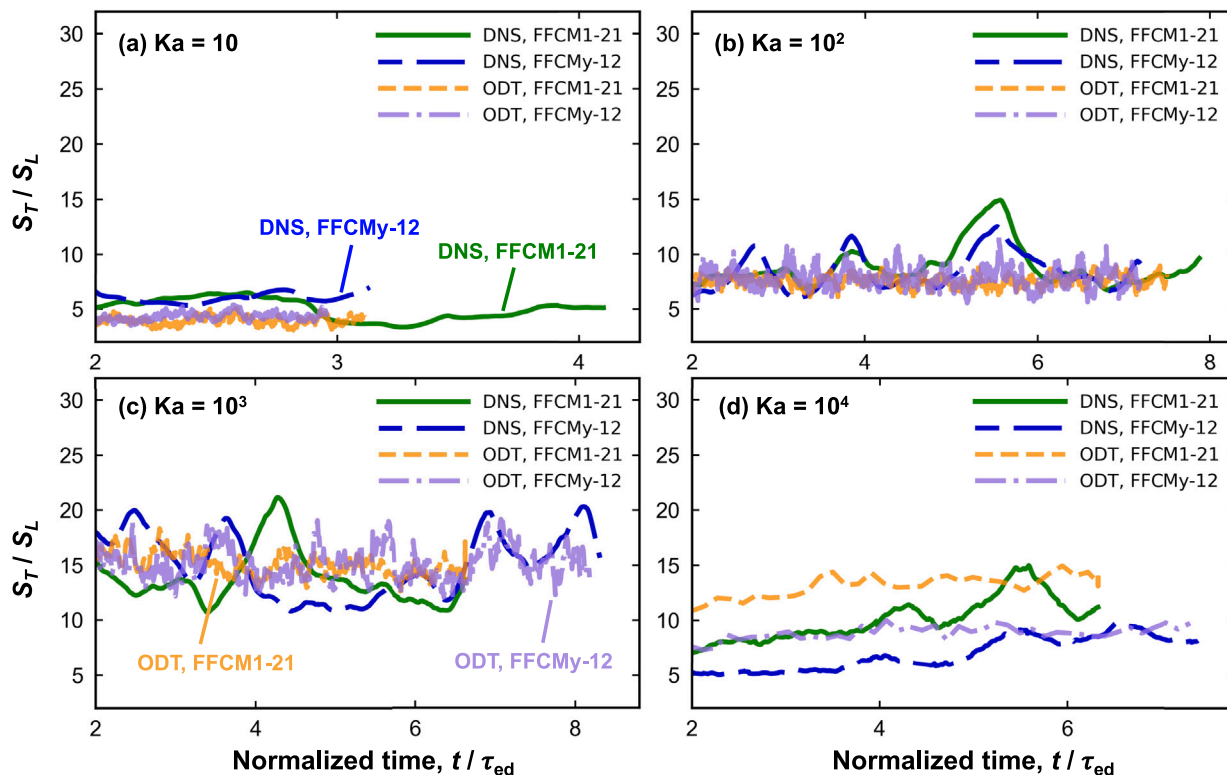
Fig. 7. Turbulent flame speed normalized by the instantaneous laminar flame speed, S_T/S_L, as a function of time normalized by the large-scale eddy turnover time, t/τ_{ed}, for (a) Ka = 10, (b) Ka = 10^2, (c) Ka = 10^3, and (d) Ka = 10^4. Solid lines: DNS using FFCM1-21; long dashed lines: DNS using FFCMy-12; dashed lines: ODT using FFCM1-21; dashed-dotted lines: ODT using FFCMy-12.

results from both models suggest that the average turbulent flame speed increases from Ka = 10 to 10^3 and subsequently drops at Ka = 10^4.

Values of the normalized S_T/S_L obtained in DNS for the two reaction models are in close agreement for Ka = 10, 10^2, and 10^3 with a maximum difference < 20%, which is similar to the difference in the laminar flame speed discussed earlier (cf. Fig. 3b). In contrast, for the Ka = 10^4 case, the difference in the average S_T/S_L obtained in DNS reaches ≈ 30% with FFCM1-21 producing higher turbulent flame speed. This could be due to the discrepancy between the two models in predicting standard combustion properties (cf. Fig. 3). More importantly, as discussed earlier, at Ka = 10^4, the turbulent flame burning weakens as the turbulent mixing time scale becomes shorter than the chemical reaction time scale. Local flame extinction and re-ignition could occur more frequently than at lower Ka. We will see that this local extinction and re-ignition phenomena can be an important factor affecting the turbulent flame speed at high Ka numbers.

Fig. 8 shows the PSR temperature S-curves calculated using FFCMy-12 and FFCM1-21 for the DNS of the CH$_4$-air flames at $\phi = 0.7$, $p = 30$ atm, and six inlet temperatures, T_{inl}, ranging from 1600 K to 2100 K. Selected inlet temperature values correspond to the range of turbulent flame conditions with significant heat release (cf. Fig. 6d and 6h). It can be seen that the S-curves gradually transform from a folded shape towards a stretched shape as the temperature rises from 1600 K to 2100 K. Note that for the folded S-curves, residence times corresponding to the turning points of the upper and lower branches are defined as the extinction residence time, τ_{ext}, and ignition residence time, τ_{ign}, respectively [56]. Shorter τ_{ext} and τ_{ign} both indicate a combustion system with a higher chemical reactivity. More specifically, a combustion system with a shorter τ_{ext} is more resistant to mixing-induced extinction, while a reaction system with a shorter τ_{ign} is more susceptible to autoignition. For the stretched S-curves (Fig. 8e and 8f), no turning points are present, which indicates even higher reactivity without extinction.

Comparison of the temperature S-curves calculated using the two models in Fig. 8 demonstrates key factors that lead to the difference in S_T/S_L at Ka = 10^4 observed earlier. In the folded S-curves in Fig. 8a–8c, FFCM1-21 predicts shorter τ_{ext} and τ_{ign}, indicating that incoming mixture is more reactive for FFCM1-21 than for FFCMy-12. We note that the shorter τ_{ext} predicted by FFCM1-21 is also observed in Fig. 3c. One exception is the ignition residence time at T_{inl} = 1600 K (Fig. 8a), however HRR is relatively low at this temperature (cf. Fig. 6d and 6h). In contrast, Fig. 8d shows that FFCM1-21 gives a stretched S-curve while FFCMy-12 still exhibits a folded S-curve. As a result, turbulent flames under similar conditions calculated with FFCMy-12 are expected to experience local extinction and re-ignition, while the same flame calculated with FFCM1-21 would behave differently due to higher reactivity. As T_{inl} rises to 2000 and 2100 K, S-curves obtained using both models become stretched, indicating burning mixtures with high chemical reactivity without extinction in this PSR configuration. This observation is corroborated by the DNS results, which give the temperature of the peak HRR around 2100 K (Fig. 6d and 6h). While the S-curve result provides a reasonable explanation to the discrepancy in S_T/S_L at Ka = 10^4, it also suggests that future model reduction procedures should consider more realistic PSR validation tests, which include tests of T_{inl} in the region of significant heat release as well as tests of not only extinction, τ_{ext}, but also ignition residence times, τ_{ign}.

The cause of the discrepancies in the prediction of τ_{ext} and τ_{ign} can be further understood using the sensitivity analysis. Fig. 9 shows ranked sensitivity spectra of τ_{ext} and τ_{ign} for the PSR calculation of a lean ($\phi = 0.7$) CH$_4$-air mixture at pressure 30 atm and 1800 K inlet temperature. Overall, the sensitivity spectra for the two models are different in two aspects. First, for both τ_{ext} and τ_{ign}, the most sensitive reactions do not overlap between the two models. Second, for FFCMy-12 (Fig. 9a), the reaction ranking for τ_{ext} is different from the ranking
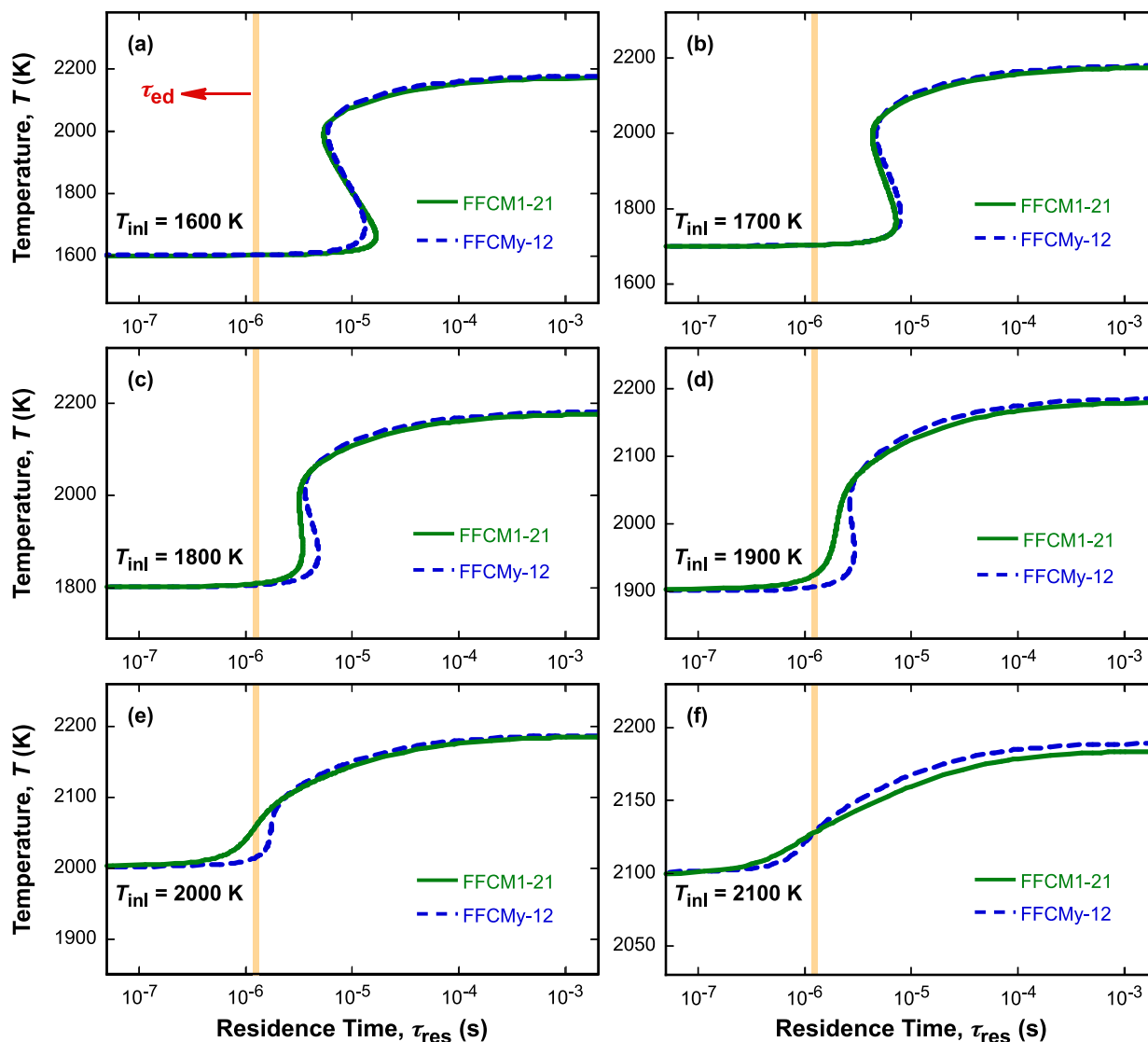
Fig. 8. Perfectly stirred reactor S-curve calculated using FFCM1-21 (solid lines) and FFCMy-12 (dashed lines) for the CH_4-air mixture at the equivalence ratio 0.7, 30 atm pressure, and (a) 1600 K, (b) 1700 K, (c) 1800 K, (d) 1900 K, (e) 2000 K, and (f) 2100 K inlet temperatures, T_{inl}. The vertical line in each figure marks the large-scale eddy turnover time, τ_{ed}, in the DNS at Ka = 10^4.

for τ_{ign}, and this is particularly true for the top 7 reactions. At the same time, for FFCM1-21, the rankings for τ_{ext} and τ_{ign} are very similar.

The differences are closely related to the mechanism reduction methodology of FFCMy-12. The sensitivity ranking difference between FFCMy-12 and FFCM1-21 primarily stems from the species that were removed as well as QSS species. In the FFCMy-12 sensitivity spectra in Fig. 9a, four irreversible reactions are highlighted, in which CH_3O and HCO are treated with the QSS assumption to immediately decompose into CH_2O + H and H + CO, respectively. Detailed reaction pathways for CH_3O and HCO are removed from FFCMy-12. In contrast, HCO reactions are important for FFCM1-21 as highlighted by the blue boxes in Fig. 9b. An earlier bifurcation analysis of dimethyl ether-air study suggested that HCO reactions such as HCO + M $\rightleftharpoons$ H + CO + M and HCO + O_2 $\rightleftharpoons$ CO + HO_2 dictate the extinction behavior of the reacting mixture in PSRs [65]. In the current study, the same two HCO reactions are found to be impactful for both extinction and ignition along with the third reaction HCO + OH $\rightleftharpoons$ H_2O + CO. This requires further investigation of the impact of HCO removal from FFCMy-12 in the future work. In addition, reactions involving CH_2 and C_2 species, which are highlighted with the orange boxes in Fig. 9b, are also prominent in

the FFCM1-21 spectra, while these two species and relevant reactions are excluded from FFCMy-12. The second observation related to the fact that in FFCMy-12 the ranking order of reactions for τ_{ext} is different from that for τ_{ign} also results from the removal of HCO chemistry leading to the elevated sensitivity to the HO_2 chemistry in FFCMy-12. In particular, reactions H + O_2 (+M) $\rightleftharpoons$ HO_2 (+M) and HO_2 + OH $\rightleftharpoons$ H_2O + O_2 are the second and third most important reactions for τ_{ext}, while they are less likely to contribute as much to τ_{ign}.

In addition to the normalized turbulent flame speed and heat release rate data, we also compared species concentration jPDF in DNS and ODT. These species include CH_4, O_2, CO_2, H_2O, H, O, OH, HO_2, and CH_2O. For the jPDF obtained from DNS, agreement between FFCM1-21 and FFCMy-12 is found for all species except HO_2 and CH_2O. We show in Figs. 10, 11, and 12 the jPDF of OH (an example where agreement is observed between the two models) as well as HO_2 and CH_2O (the two species exhibiting discrepancies between FFCM1-21 and FFCMy-12), respectively. The jPDF of the other six species are included in the Supplementary Materials Section S5.

Fig. 10 shows that jPDF of the OH radical obtained from the DNS using both FFCM1-21 and FFCMy-12 (top two rows) are very similar for
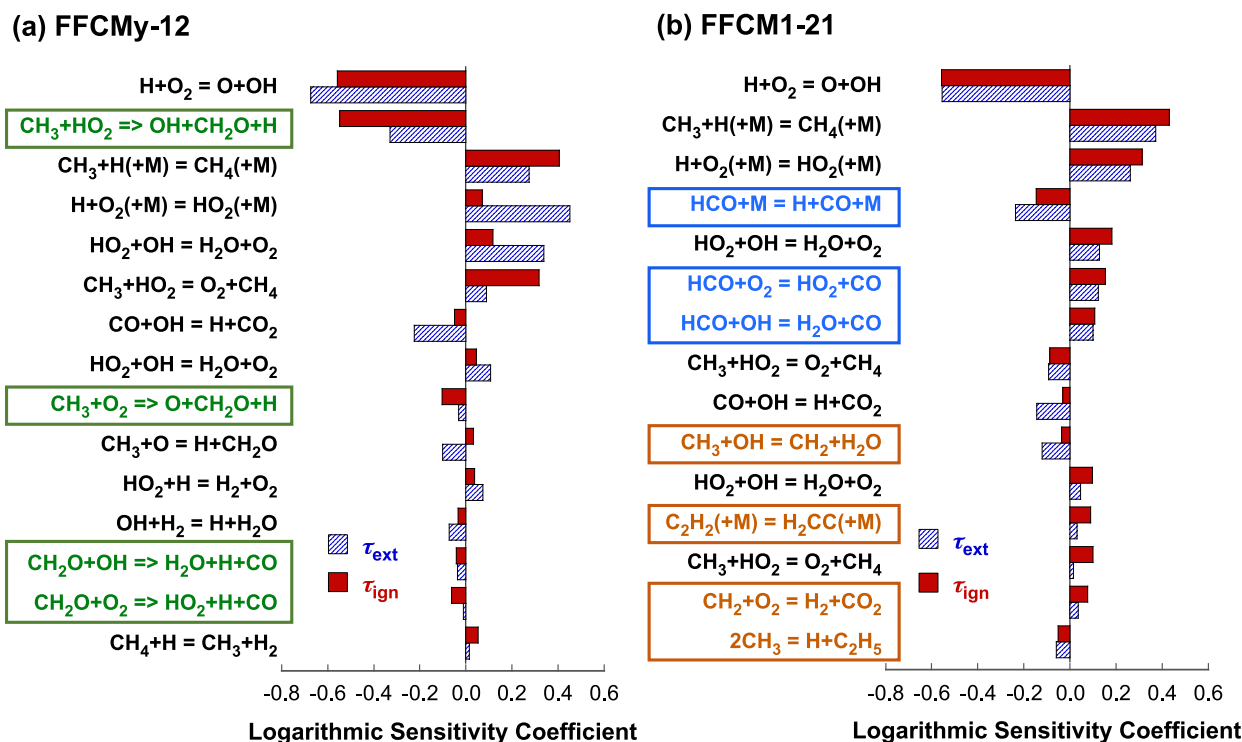
Fig. 9. Sensitivity spectra of the perfectly stirred reactor extinction, τ_{ext}, and ignition residence times, τ_{ign}, computed for the CH_4-air mixture at the equivalence ratio 0.7, 30 atm pressure, and 1800 K inlet temperature, T_{inl}, using (a) FFCMy-12 and (b) FFCM1-21 models. Reactions highlighted in panel (a) are those under the quasi-steady state assumption of HCO (replaced by H + CO in the product) and CH_3O (replaced by CH_2O + H in the product). Those reactions are treated as forward irreversible. Reactions highlighted in panel (b) are those involving HCO, CH_2, and other C_2 species in FFCM1-21 not retained in FFCMy-12.

all four Ka values considered. At the same time, however, distributions of HO_2 in DNS using FFCM1-21 and FFCMy-12 differ considerably (Fig. 11, top two rows), which can be seen both in the laminar profiles as well as turbulent scatters of the jPDF (and their means). Again, the difference results from the coupled effects of species elimination, QSS treatment, and rate constant adjustments. In particular, the peculiar rise of HO_2 concentrations at around 1000–1500 K seen in Figs. 11e–h (the second row) is primarily due to the elimination of H_2O_2 from FFCMy-12. Since HO_2 is relatively stable in this temperature range, its concentration will accumulate in the absence of a major destruction sink, H_2O_2.

Similarly, differences are seen in the jPDF of CH_2O obtained in DNS using FFCM1-21 and FFCMy-12 (Fig. 12, top two rows). In particular, at high Ka numbers 10^3 and 10^4, the two FFCM models again produce two distinctive characteristics of CH_2O concentrations. The jPDF generated by FFCMy-12 DNS deviate further from their respective laminar flame profiles than the FFCM1-21 jPDF. The qualitative cause of such difference is again multi-fold. For example, the QSS treatment of CH_3O boosts the production rate of CH_2O. On the contrary, the QSS treatment of HCO increases the destruction rate of CH_2O, since the original reaction of CH_2O + R ⇌ RH + HCO would become irreversible CH_2O + R ⇒ RH + H + CO, which would impede the production of CH_2O through the reverse reaction (see Table S1 in SM Section S2).

In summary, FFCMy-12 performs as well as FFCM1-21 for most conditions in high-Ka turbulent combustion DNS. Some discrepancies start to occur at extreme conditions, where intense turbulent mixing impedes chemical reactions and heat release. Under such conditions, FFCMy-12 tends to predict lower reactivity due to the overestimates of local extinction and re-ignition as compared to FFCM1-21. The PSR and sensitivity analyses suggest that future reduced model development should pay particular attention to PSR conditions, where extinction and re-ignition merge (the transition between folded and stretched S-curves). Therefore, since extinction residence time in PSR is already

a common validation target, it is equally important to consider the ignition residence time.

4.2. Comparison of the ODT model and DNS

Reaction model reduction typically uses legacy, laminar combustion properties as targets. Turbulent flames can generate a significantly broader thermochemical state space because of local mixing (including exhaust gas recirculation), extinction, and re-ignition. For this reason, a reaction model reduced and tested against a prescribed set of legacy combustion properties may not reproduce accurately the kinetic behavior in turbulent flames. To this end, one-dimensional turbulence (ODT) modeling could potentially offer a tool to validate reduced models and understand their limitations, provided that the Ka number is not excessively high.

In the companion paper Part I [51], we compared the ODT modeling results with DNS using only the FFCM1-21 skeletal model. Here in Part II, we consider FFCMy-12 and show that the ODT model can reproduce the turbulent flame speeds (Fig. 7) and the mean normalized heat release rates (Fig. 6) observed in DNS for Ka ≤ 10^3, even though the ODT jPDF tend to be broader than the DNS results at the lowest and highest Ka values considered. At a more detailed level, the ODT model largely reproduces the mean of the jPDF distributions of the mass fractions of the major species CH_4 (Fig. S11), O_2 (Fig. S12), CO_2 (Fig. S13), and H_2O (Fig. S14), along with minor radical species OH (Fig. 10), H (Fig. S15), and O (Fig. S16), although the ODT jPDF for these radical species are also broader than those in DNS. Similar observations can be made for other minor species HO_2 and CH_2O in Figs. 11 and 12, respectively. At Ka = 10^4, discrepancies are found between the ODT and DNS in terms of the mean and scatter of the jPDF distributions of the radical species, namely OH (Fig. 10), HO_2 (Fig. 11), CH_2O (Fig. 12), H (Fig. S15), and O (Fig. S16). The divergence of ODT from DNS at high Karlovitz numbers is consistent with the trends
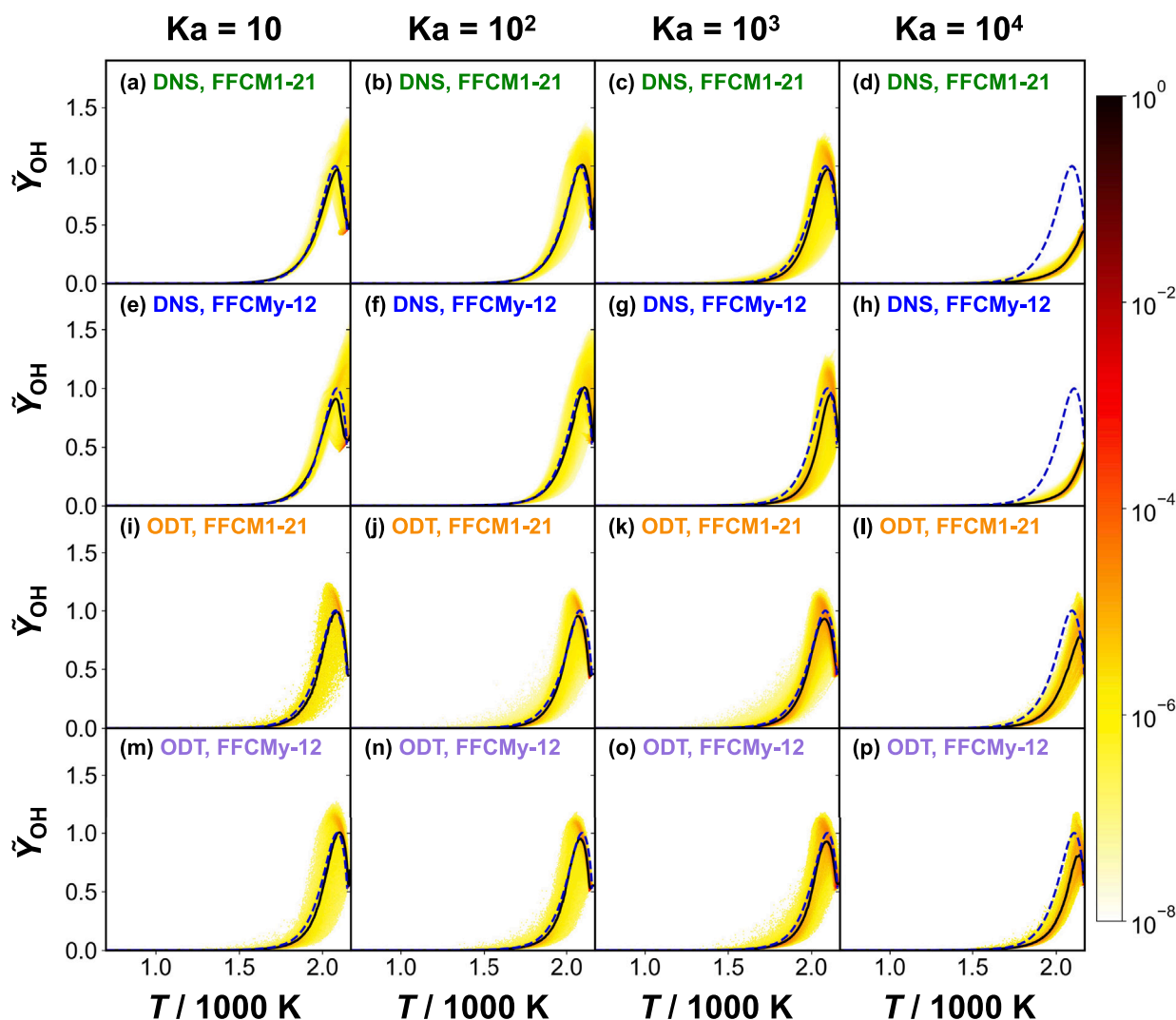
Fig. 10. Joint probability density function (jPDF) of the normalized OH mass fraction, $\tilde{Y}_{OH}$, vs. temperature obtained from DNS with FFCM1-21 (first row, panels a–d), DNS with FFCMy-12 (second row, panels e–h), ODT with FFCM1-21 (third row, panels i–l), and ODT with FFCMy-12 (bottom row, panels m-p). The jPDF is computed at Ka = 10 (first column, panels a, e, i, m), Ka = 10^2 (second column, panels b, f, j, n), Ka = 10^3 (third column, panels c, g, k, o), and Ka = 10^4 (fourth column, panels d, h, l, p). Solid lines: mean of the jPDF; dashed lines: results obtained from the laminar premixed flame computation.

identified in the companion paper Part I [51], and the readers are referred to the detailed discussion there [51]. Briefly, with increasing Ka, multi-dimensional effects become stronger thus possibly accounting for the difference seen between the ODT and DNS. Nevertheless, the results shown here and the companion paper Part I [51] indicate that the ODT model is a promising tool for a rather inexpensive validation of the reduced reaction models, considering validation targets such as turbulent flame speed, distribution of heat release rate and species concentration, and additional targets such as the time-averaged flame structure. We envision that in the future streamlined reaction model reduction schemes, the ODT model can serve such a purpose satisfactorily. For example, future work should address whether using ODT in addition to the standard model reduction methods will lead to an improvement in the reduced reaction model.

5. Conclusions

In the present study, FFCMy-12, a 12-species reduced reaction model for CH_4 combustion was developed for turbulent combustion modeling over a wide range of regimes from moderate to very high Karlovitz numbers. A previously developed skeletal model, FFCM1-21, was used as a benchmark to evaluate the performance of FFCMy-12.

FFCMy-12 was first tested in zero- and one-dimensional combustion systems based on the calculated ignition delay times, laminar flame speeds, perfectly stirred reactor extinction and ignition residence times, and burned product temperature evolution in a rocket nozzle flow expansion. Most of the test cases show agreement between FFCMy-12 and FFCM1-21, though some discrepancies are observed, which are due to further reduction performed to generate FFCMy-12. Furthermore, both models were then tested in the three-dimensional DNS computations of turbulent flames at medium to high Karlovitz numbers. FFCMy-12 was capable of predicting turbulent flame speed, heat release rate, and major species concentrations at Ka = $10 - 10^3$, while deviations from FFCM1-21 were observed at Ka = 10^4. The discrepancies stem from the removal and modification of species and associated reaction parameters, which are sensitive to the local extinction and re-ignition processes.

Finally, we conclude that (1) the one-dimensional turbulent (ODT) model presented in the companion paper (Part I) can serve as a practical surrogate for DNS and an efficient tool for testing and validating chemical reaction model reduction; (2) future reaction model reduction workflow should consider both local flame extinction and re-ignition under relevant conditions.
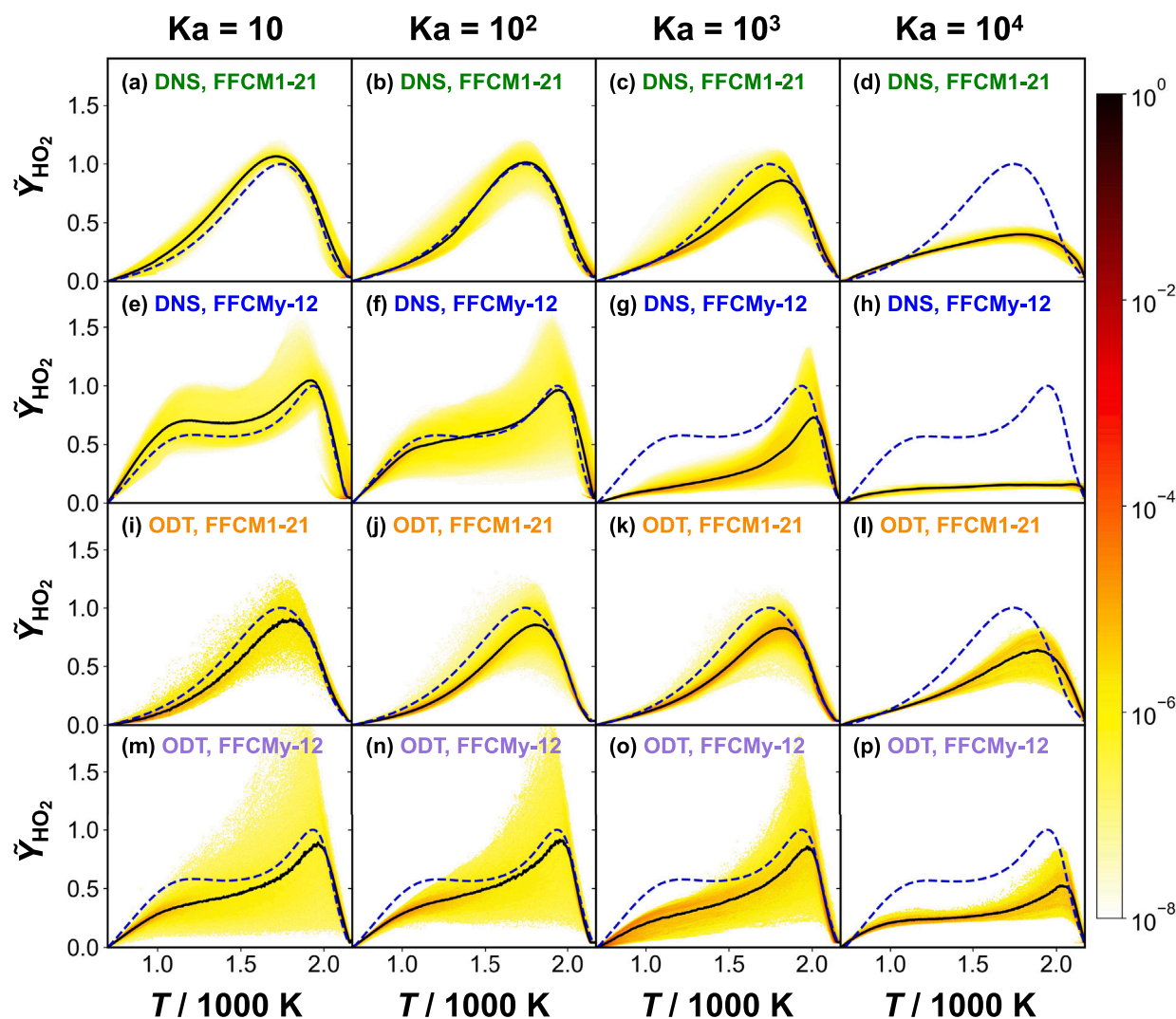
Fig. 11. Joint probability density function (jPDF) of the normalized HO_2 mass fraction, $\tilde{Y}_{HO_2}$, vs. temperature obtained from DNS with FFCM1-21 (first row, panels a–d), DNS with FFCMy-12 (second row, panels e–h), ODT with FFCM1-21 (third row, panels i–l), and ODT with FFCMy-12 (bottom row, panels m–p). The jPDF is computed at Ka = 10 (first column, panels a, e, i, m), Ka = 10^2 (second column, panels b, f, j, n), Ka = 10^3 (third column, panels c, g, k, o), and Ka = 10^4 (fourth column, panels d, h, l, p). Solid lines: mean of the jPDF; dashed lines: results obtained from the laminar premixed flame computation.

CRediT authorship contribution statement

Rui Xu: Designed research, Wrote the original draft, Developed the 12-species reduced methane oxidation model, Contributed to the review and editing phases of the manuscript. **Sai Sandeep Dammati:** Performed DNS, Contributed to the review and editing phases of the manuscript. **Xian Shi:** Performed the rocket nozzle expansion simulation, Contributed to the review and editing phases of the manuscript. **Ethan Samuel Genter:** Performed the detonation simulation, Contributed to the review and editing phases of the manuscript. **Zoltan Jozefik:** Performed ODT simulations, Contributed to the review and editing phases of the manuscript. **Matthew E. Harvazinski:** Performed ODT simulations, Contributed to the review and editing phases of the manuscript. **Tianfeng Lu:** Developed the 21-species skeletal methane oxidation model, Contributed to the review and editing phases of the manuscript. **Alexei Y. Poludnenko:** Performed DNS, Contributed to the review and editing phases of the manuscript. **Venkateswaran Sankaran:** Performed ODT simulations, Contributed to the review and editing phases of the manuscript. **Alan R. Kerstein:** Contributed to the ODT formulation and result analysis, Contributed to the review and editing phases of the manuscript. **Hai Wang:** Designed research, Wrote the original draft, Contributed to the review and editing phases of the manuscript.

Declaration of competing interest

The authors declare that they have no known competing financial interests or personal relationships that could have appeared to influence the work reported in this paper.
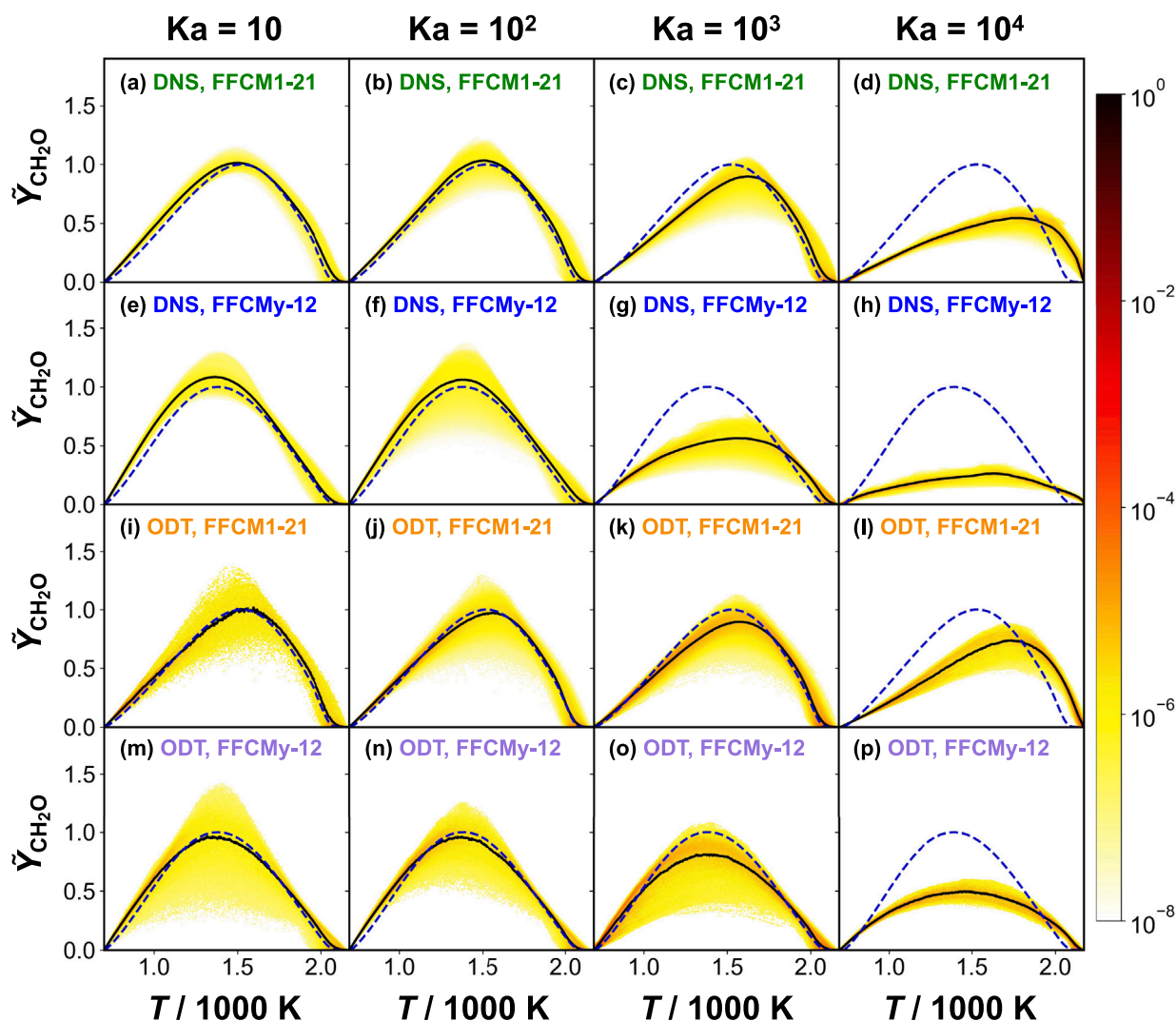
Acknowledgments

Fig. 12. Joint probability density function (jPDF) of the normalized CH_2O mass fraction, $\tilde{Y}_{CH_2O}$, vs. temperature obtained from DNS with FFCM1-21 (first row, panels a–d), DNS with FFCMy-12 (second row, panels e–h), ODT with FFCM1-21 (third row, panels i–l), and ODT with FFCMy-12 (bottom row, panels m–p). The jPDF is computed at Ka = 10 (first column, panels a, e, i, m), Ka = 10^2 (second column, panels b, f, j, n), Ka = 10^3 (third column, panels c, g, k, o), and Ka = 10^4 (fourth column, panels d, h, l, p). Solid lines: mean of the jPDF; dashed lines: results obtained from the laminar premixed flame computation.

Appendix A. Supplementary data

Supplementary material related to this article can be found online at https://doi.org/10.1016/j.combustflame.2024.113380.

References

[1] H. Pitsch, Large-eddy simulation of turbulent combustion, Annu. Rev. Fluid Mech. 38 (2006) 453–482.

[2] A.M. Steinberg, P.E. Hamlington, X. Zhao, Structure and dynamics of highly turbulent premixed combustion, Prog. Energy Combust. Sci. 85 (2021) 100900.

[3] A. Aspden, J. Bell, M. Day, F. Egolfopoulos, Turbulence–flame interactions in lean premixed dodecane flames, Proc. Combust. Inst. 36 (2017) 2005–2016.

[4] B. Savard, B. Bobbitt, G. Blanquart, Structure of a high karlovitz n-C_7H_{16} premixed turbulent flame, Proc. Combust. Inst. 35 (2015) 1377–1384.

[5] H. Wang, E.R. Hawkes, J.H. Chen, Turbulence-flame interactions in DNS of a laboratory high karlovitz premixed turbulent jet flame, Phys. Fluids 28 (2016) 095107.

[6] H. Wang, E.R. Hawkes, J.H. Chen, A direct numerical simulation study of flame structure and stabilization of an experimental high Ka CH_4/air premixed jet flame, Combust. Flame 180 (2017) 110–123.

[7] C. Xu, A.Y. Poludnenko, X. Zhao, H. Wang, T. Lu, Structure of strongly turbulent premixed n-dodecane-air flames: Direct numerical simulations and chemical explosive mode analysis, Combust. Flame 209 (2019) 27–40.

[8] A. Aspden, M. Day, J. Bell, Lewis number effects in distributed flames, Proc. Combust. Inst. 33 (2011) 1473–1480.

[9] S. Lapointe, B. Savard, G. Blanquart, Differential diffusion effects, distributed burning, and local extinctions in high karlovitz premixed flames, Combust. Flame 162 (2015) 3341–3355.

[10] B. Savard, G. Blanquart, Broken reaction zone and differential diffusion effects in high karlovitz n-C_7H_{16} premixed turbulent flames, Combust. Flame 162 (2015) 2020–2033.

[11] S. Lapointe, G. Blanquart, Fuel and chemistry effects in high karlovitz premixed turbulent flames, Combust. Flame 167 (2016) 294–307.

[12] D. Dasgupta, W. Sun, M. Day, A.J. Aspden, T. Lieuwen, Analysis of chemical pathways and flame structure for n-dodecane/air turbulent premixed flames, Combust. Flame 207 (2019) 36–50.

[13] X. Zhao, Y. Tao, T. Lu, H. Wang, Sensitivities of direct numerical simulations to chemical kinetic uncertainties: spherical flame kernel evolution of a real jet fuel, Combust. Flame 209 (2019) 117–132.

[14] H. Wang, E.R. Hawkes, J.H. Chen, B. Zhou, Z. Li, M. Aldén, Direct numerical simulations of a high karlovitz number laboratory premixed jet flame–an analysis of flame stretch and flame thickening, J. Fluid Mech. 815 (2017) 511–536.

[15] A. Aspden, M. Day, J. Bell, Turbulence–flame interactions in lean premixed hydrogen: transition to the distributed burning regime, J. Fluid Mech. 680 (2011) 287–320.

[16] A. Aspden, M. Day, J. Bell, Towards the distributed burning regime in turbulent premixed flames, J. Fluid Mech. 871 (2019) 1–21.

[17] R. Darragh, C.A. Towery, A.Y. Poludnenko, P.E. Hamlington, Particle pair dispersion and eddy diffusivity in a high-speed premixed flame, Proc. Combust. Inst. 38 (2021) 2845–2852.

[18] A.S. Tomlin, T. Turányi, M.J. Pilling, Mathematical tools for the construction, investigation and reduction of combustion mechanisms, in: Comprehensive Chemical Kinetics, vol. 35, Elsevier, 1997, pp. 293–437.

[19] H. Rabitz, M. Kramer, D. Dacol, Sensitivity analysis in chemical kinetics, Annu. Rev. Phys. Chem. 34 (1983) 419–461.

[20] T. Turányi, Sensitivity analysis of complex kinetic systems. Tools and applications, J. Math. Chem. 5 (1990) 203–248.

[21] S. Vajda, P. Valko, T. Turanyi, Principal component analysis of kinetic models, Int. J. Chem. Kinet. 17 (1985) 55–81.

[22] B. Bhattacharjee, D.A. Schwer, P.I. Barton, W.H. Green, Optimally-reduced kinetic models: reaction elimination in large-scale kinetic mechanisms, Combust. Flame 135 (2003) 191–208.

[23] H. Wang, M. Frenklach, Detailed reduction of reaction mechanisms for flame modeling, Combust. Flame 87 (1991) 365–370.

[24] T. Lu, C.K. Law, A directed relation graph method for mechanism reduction, Proc. Combust. Inst. 30 (2005) 1333–1341.

[25] T. Lu, C.K. Law, On the applicability of directed relation graphs to the reduction of reaction mechanisms, Combust. Flame 146 (2006) 472–483.

[26] T. Lu, C.K. Law, Linear time reduction of large kinetic mechanisms with directed relation graph: *n*-heptane and *iso*-octane, Combust. Flame 144 (2006) 24–36.

[27] P. Pepiot-Desjardins, H. Pitsch, An efficient error-propagation-based reduction method for large chemical kinetic mechanisms, Combust. Flame 154 (2008) 67–81.

[28] R. Sankaran, E.R. Hawkes, J.H. Chen, T. Lu, C.K. Law, Structure of a spatially developing turbulent lean methane–air bunsen flame, Proc. Combust. Inst. 31 (2007) 1291–1298.

[29] X. Zheng, T. Lu, C.K. Law, Experimental counterflow ignition temperatures and reaction mechanisms of 1,3-butadiene, Proc. Combust. Inst. 31 (2007) 367–375.

[30] J.-Y. Chen, A general procedure for constructing reduced reaction mechanisms with given independent relations, Combust. Sci. Technol. 57 (1988) 89–94.

[31] C.J. Sung, C. Law, J.-Y. Chen, Augmented reduced mechanisms for NO emission in methane oxidation, Combust. Flame 125 (2001) 906–919.

[32] T. Lövås, F. Mauss, C. Hasse, N. Peters, Development of adaptive kinetics for application in combustion systems, Proc. Combust. Inst. 29 (2002) 1403–1410.

[33] H.S. Soyhan, F. Mauss, C. Sorusbay, Chemical kinetic modeling of combustion in internal combustion engines using reduced chemistry, Combust. Sci. Technol. 174 (2002) 73–91.

[34] T. Mendiara, M. Alzueta, A. Millera, R. Bilbao, An augmented reduced mechanism for methane combustion, Energy Fuels 18 (2004) 619–627.

[35] A. Massias, D. Diamantis, E. Mastorakos, D.A. Goussis, An algorithm for the construction of global reduced mechanisms with CSP data, Combust. Flame 117 (1999) 685–708.

[36] A. Massias, D. Diamantis, E. Mastorakos, D.A. Goussis, Global reduced mechanisms for methane and hydrogen combustion with nitric oxide formation constructed with CSP data, Combust. Theory Model. 3 (1999) 233.

[37] T. Lu, Y. Ju, C.K. Law, Complex CSP for chemistry reduction and analysis, Combust. Flame 126 (2001) 1445–1455.

[38] C.J. Montgomery, C. Yang, A.R. Parkinson, J.-Y. Chen, Selecting the optimum quasi-steady-state species for reduced chemical kinetic mechanisms using a genetic algorithm, Combust. Flame 144 (2006) 37–52.

[39] T. Lu, C.K. Law, Systematic approach to obtain analytic solutions of quasi steady state species in reduced mechanisms, J. Phys. Chem. A 110 (2006) 13202–13208.

[40] T. Lu, C.K. Law, A criterion based on computational singular perturbation for the identification of quasi steady state species: A reduced mechanism for methane oxidation with NO chemistry, Combust. Flame 154 (2008) 761–774.

[41] U. Maas, S.B. Pope, Simplifying chemical kinetics: Intrinsic low-dimensional manifolds in composition space, Combust. Flame 88 (1992) 239–264.

[42] S.-H. Lam, D.A. Goussis, Understanding complex chemical kinetics with computational singular perturbation, Symp. Int. Combust. 22 (1989) 931–941.

[43] S.-H. Lam, D.A. Goussis, The CSP method for simplifying kinetics, Int. J. Chem. Kinet. 26 (1994) 461–486.

[44] M. Valorani, H.N. Najm, D.A. Goussis, CSP analysis of a transient flame-vortex interaction: time scales and manifolds, Combust. Flame 134 (2003) 35–53.

[45] M. Valorani, F. Creta, D.A. Goussis, J.C. Lee, H.N. Najm, An automatic procedure for the simplification of chemical kinetic mechanisms based on CSP, Combust. Flame 146 (2006) 29–51.

[46] Y. Zhang, W. Dong, L. Vandewalle, R. Xu, G. Smith, H. Wang, Foundational fuel chemistry model version 2.0 (FFCM-2), 2023, https://web.stanford.edu/group/haiwanglab/FFCM2.

[47] Y. Zhang, W. Dong, L.A. Vandewalle, R. Xu, G.P. Smith, H. Wang, Neural network approach to response surface development for reaction model optimization and uncertainty minimization, Combust. Flame 251 (2023) 112679.

[48] Y. Zhang, W. Dong, R. Xu, G.P. Smith, H. Wang, Foundational fuel chemistry model 2 – *iso*-Butene chemistry and application in modeling alcohol-to-jet fuel combustion, Combust. Flame 259 (2024) 113168.

[49] G.P. Smith, Y. Tao, H. Wang, Foundational fuel chemistry model version 1.0 (FFCM-1), 2016, https://web.stanford.edu/group/haiwanglab/FFCM1/pages/FFCM1.html.

[50] Y. Tao, G.P. Smith, H. Wang, Critical kinetic uncertainties in modeling hydrogen/carbon monoxide, methane, methanol, formaldehyde, and ethylene combustion, Combust. Flame 195 (2018) 18–29.

[51] Z. Jozefik, M.E. Harvazinski, V. Sankaran, S.S. Dammati, A.Y. Poludnenko, T. Lu, A.R. Kerstein, R. Xu, H. Wang, Modeling of high-speed, methane-air, turbulent combustion, Part I: One-dimensional turbulence modeling with comparison to DNS, Combust. Flame 263 (2024) 113379.

[52] R.J. Kee, F.M. Rupley, J.A. Miller, Chemkin-II: A Fortran chemical kinetics package for the analysis of gas-phase chemical kinetics, Tech. Rep. SAND-89-8009, Sandia National Labs., Livermore, CA (USA), 1989.

[53] A.E. Lutz, R.J. Kee, J.A. Miller, SENKIN: A FORTRAN program for predicting homogeneous gas phase chemical kinetics with sensitivity analysis, Tech. Rep.SAND-87-8248, Sandia National Labs., Livermore, CA (USA), 1988.

[54] R.J. Kee, J.F. Grcar, M.D. Smooke, J.A. Miller, E. Meeks, PREMIX: a Fortran program for modeling steady laminar one-dimensional premixed flames, Tech. Rep. SAND85-8249, Sandia National Labs., Livermore, CA (USA), 1985.

[55] P. Glarborg, R.J. Kee, J.F. Grcar, J.A. Miller, PSR: A FORTRAN program for modeling well-stirred reactors, Tech. Rep. SAND86-8209, Sandia National Labs., Livermore, CA (USA), 1986.

[56] C.K. Law, Combustion Physics, Cambridge University Press, 2010.

[57] J. Warnatz, The structure of laminar alkane-, alkene-, and acetylene flames, Symp. Int. Combust. 18 (1981) 369–384.

[58] D.G. Goodwin, H.K. Moffat, I. Schoegl, R.L. Speth, B.W. Weber, Cantera: An object-oriented software toolkit for chemical kinetics, thermodynamics, and transport processes, 2022, http://dx.doi.org/10.5281/zenodo.6387882, https://www.cantera.org Version 2.6.0.

[59] A.Y. Poludnenko, E.S. Oran, The interaction of high-speed turbulence with flames: Global properties and internal flame structure, Combust. Flame 157 (2010) 995–1011.

[60] A.Y. Poludnenko, E.S. Oran, The interaction of high-speed turbulence with flames: Turbulent flame speed, Combust. Flame 158 (2011) 301–326.

[61] G.P. Smith, Y. Zhang, H. Wang, Foundational fuel chemistry model development version y (FFCMy), 2018, personal communications.

[62] C.K. Westbrook, F.L. Dryer, Simplified reaction mechanisms for the oxidation of hydrocarbon fuels in flames, Combust. Sci. Technol. 27 (1981) 31–43.

[63] G.P. Smith, D.M. Golden, M. Frenklach, N.W. Moriarty, B. Eiteneer, M. Goldenberg, C.T. Bowman, R.K. Hanson, S. Song, W.C. Gardiner Jr., V.V. Lissianski, Z. Qin, GRI-mech 3.0, 1999, http://combustion.berkeley.edu/gri-mech/version30/text30.html.

[64] H. Wang, X. You, A.V. Joshi, S.G. Davis, A. Laskin, F. Egolfopoulos, C.K. Law, USC mech version II. High-temperature combustion reaction model of H_2/CO/C_1-C_4 compounds, 2007, https://ignis.usc.edu:80/Mechanisms/USC-Mech%20II/USC_Mech%20II.htm.

[65] R. Shan, T. Lu, A bifurcation analysis for limit flame phenomena of DME/air in perfectly stirred reactors, Combust. Flame 161 (2014) 1716–1723.